Fundamentals of tin iodide perovskites

Filippetti, A.; Kahmann, S.; Caddeo, C.; Mattoni, A.; Saba, M.; Bosin, A.; Loi, M. A.

Published in:
Journal of Materials Chemistry A

DOI:
10.1039/d1ta01573g

Publication date:
2021

Journal of Materials Chemistry A

ROYAL SOCIETY OF CHEMISTRY

PAPER

View Article Online
View Journal | View Issue

Cite this: J. Mater. Chem. A, 2021, 9, 11812

Fundamentals of tin iodide perovskites: a promising route to highly efficient, lead-free solar cells†

A. Filippetti, *[ab] S. Kahmann, ‡[c] C. Caddeo, [b] A. Mattoni, [b] M. Saba, [a] A. Bosin [a] and M. A. Loi [c]

Received 22nd February 2021
Accepted 29th April 2021

DOI: 10.1039/d1ta01573g

rsc.li/materials-a

Hybrid tin-iodide perovskites are investigated as potential lead-free replacement of the lead-iodide perovskites; however, the intrinsic operational limit of these systems has not been described in detail, so far. In this work we combine advanced *ab initio* calculations with XRD and absorption measurements to lay out the fundamentals of formamidinium ($FASnI_3$) and methylammonium ($MASnI_3$) tin iodide perovskites, in comparison with the lead-halide $MAPbI_3$ prototype. Our theoretical analysis reveals that the tin-based materials display an intrinsic photoconversion efficiency on a par with the lead perovskites, and even superior in the thick-layer limit, where the theoretical PCE reaches 30.5% for lead-halides, and 32.3% for tin-halides under AM1.5G illumination; this is the result of two competing factors: a smaller absorption cross section at the onset for stannates, and their smaller band gap of 1.36 eV, thus very close to the ideal Shockley–Queisser limit. We found the rate of photoluminescence emission extremely sensitive to the absorption spectral weight at the band extrema, resulting in *B*-factor as different as 7.6×10^{-9} s^{-1} cm^3 for $MASnI_3$ and 0.4×10^{-10} s^{-1} cm^3 for $FASnI_3$. The additional impact of Urbach energy and hole doping, giving rise to large Burstein–Moss effect, is described in detail.

1. Introduction

The success of lead-halide perovskites for highly efficient photovoltaic solar cells[1–5] stems from a series of fundamental aspects characterizing electronic, optical, and transport properties. A pronounced defect tolerance and the absence of deep trap states are commonly seen as crucial aspects,[6–21] together with the modest incidence of bound excitons.[22–26] However, the intrinsic aspects are similarly crucial in making these materials special: inorganic materials with a direct, narrow band gap and large optical absorption at the band edge are anything but easy to find, and such a fortuitous occurrence has a lot to do with the presence of lead at the B site of the ABX_3 perovskite structure. In fact, the character of the band gap, and ultimately, the large optical absorption coefficient, are largely set by the intra-atomic 6s-to-5p optical transition from the Pb^{2+} ion. It is not surprising, then, that replacing Pb with a less toxic element capable of retaining the performance of lead halides has so far proven to be complicated, and that, despite a large variety of efforts in different directions, the best options to the aim remain the single B-site substitution with the chemical analogues Sn or Ge.

Tin-halide perovskites have been the subject of great interest in the community,[27–31] since most of their basic properties appear similar, or even superior to that of their lead-based counterparts,[32–36] including an almost ideal band gap energy according to the Shockley–Queisser (SQ) limit, and the direct formation of free charge carriers.[35,36] Even more fascinating is the reported optical emission by hot carriers,[35] which may be used to overcome the SQ efficiency limit.[37] At odds with these high expectations, the conversion efficiency reported for tin-based perovskites remained for several years anchored to about 6%,[27] thus well below the record value of ~25% recently reached by the lead-based prototype.[38] The low efficiency is understood to be primarily a consequence of the Sn^{2+} to Sn^{4+} oxidation tendency, which has the effect to introduce an amount of unintentional hole doping concentration, estimated to be at least 5×10^{17} cm^{-3},[32–35] causing large recombination losses and deteriorating the ideal perovskite behavior. In the last few years, several strategies to reduce or suppress oxidation have been attempted, based on substitutional doping or the use of additives such as SnI_2 and SnF_2, with apparently promising results.[39–53] Nowadays, the maximum reported efficiency exceeds 10%,[48–54] upon suited doping treatment and solvent engineering. On the other hand, it was put in evidence that the enhanced recombination due to native doping can be conveniently exploited in lasing application, generating the

[a]Dipartimento di Fisica, Università di Cagliari, S.P. Monserrato-Sestu Km. 0700, Monserrato, CA, 09042-I, Italy. E-mail: alessio.filippetti@dsf.unica.it

[b]Consiglio Nazionale delle Ricerche, Istituto Officina dei Materiali, CNR-IM, Cagliari, Cittadella Universitaria, Monserrato 09042-I, CA, Italy

[c]Zernike Institute for Advanced Materials, University of Groningen, Nijenborgh 4, 9747 AG Groningen, The Netherlands

† Electronic supplementary information (ESI) available. See DOI: 10.1039/d1ta01573g

‡ Current address: Cavendish Laboratory, University of Cambridge, JJ Thomson Avenue, CB30HE Cambridge, UK, sk2133@cam.ac.uk

achievement of amplified spontaneous emission for charge injection as low as 8×10^{17} cm^{-3}.[32]

While it is unquestionable that tin-halide perovskites presently grown in the lab deviate much more than lead-halides from a purely intrinsic behavior, it is of the outmost importance to evaluate the intrinsic level of their properties to judge whether further engineering efforts could at least in theory offer comparable device performance. To this aim, *ab initio* calculations are a valuable tool, which provides a reliable term of comparison to the experimental analysis. However, for reasons related to the methodological aspects (described in Section 2) the theoretical literature on tin-halide perovskites is significantly less copious than what is available for lead halides. To fill this gap, in this work we deliver what is, to our knowledge, the first extended theoretical investigation of tin halide perovskites encompassing structural, electronic, optical, recombination, and photoconversion properties, all described in the framework of a single, unified theoretical approach able to overcome the deficiencies of the standard *ab initio* theory. Our aim is providing, on the one hand, a clear understanding of the fundamental mechanisms ruling the tin-halide perovskite behavior, and, on the other, a back-to-back comparison of experiments and theory, useful to quantify the separation between the currently available material and the idealized behavior which could be hopefully approached through future progress in processing.

2. Methods

It is well known that the standard *ab initio* approach based on Density Functional Theory (DFT) is affected by severe systematic errors concerning the determination of the electronic properties. A few advanced approaches overcoming the DFT deficiencies are nowadays available to the community. Typically, however, they are highly computationally demanding, up to the point of being hardly practicable for large-size systems. In this work we use a method, the variational pseudo self-interaction correction approach (VPSIC),[55] which over the years has demonstrated to satisfy both accuracy and computational feasibility for large-size systems such as superlattices[56–58] and surfaces,[59] and was recently applied to Ge-based hybrid perovskites[60] and In/Ag double perovskites.[61] The VPSIC removes the main DFT deficiency, namely the electronic self-interaction (SI) present in the single particle potential. The SI is a blessing from computational viewpoint, since it causes the electronic potential to be local, and is at the root of the powerful simplicity of the DFT approach. On the other hand, for rather ionic materials, the SI generates large inaccuracies in the electronic energies (especially for localized charges) and a systematic underestimation of the band gap. A remarkable exception are lead-halide perovskites, for whom the large spin–orbit coupling (SOC) of Pb and the SI error of the band gap (both on the order of ~1 eV) largely compensate each other due to their opposite sign, thus conveying a DFT band gap, calculated without SOC contribution, in almost perfect agreement with the measurement. This fortuitous compensation does not apply to stannates, since SOC for Sn is too small (~0.1 eV); it follows that calculations carried out by standard local functionals[62,63] predict band gaps underestimated by 50% or more, while a reliable description of the electronic properties requires to operate beyond the DFT level. Up until today only a handful of beyond-DFT calculations have been proposed, carried out using the GW approach[64] or hybrid energy functionals.[64–66] Those are both accurate methods but require massive computational workload which discourages their application on a large scale. The VPSIC approach used in this work was shown to be of accuracy similar to the very popular hybrid HSE hybrid functional,[67,68] albeit substantially less computationally demanding. An interesting alternative is represented by the DFT-1/2 method,[69] which was recently used for stannates,[70–72] and can be considered a simplified version of the VPSIC (a comparison of these two approaches can be found in ref. 73).

The VPSIC method is implemented in the freeware PWSIC code, written and owned by the authors;[74] the code exploits plane-wave basis set and ultrasoft pseudopotentials[75] to describe the electron–ion interaction. For all the calculations, a cut-off energy of 40 Ry was used. Atomic positions are fully relaxed within a force threshold of 10^{-4} Ha Bohr^{-1}. Self-consistent electronic structure and density of states are calculated on dense $20 \times 20 \times 20$ k-point grid, further interpolated by linear tetrahedron method; the optical functions are calculated in random-phase approximation on ultra-dense k-point mesh of more than 5000 *ab initio* k-points. This high precision of k-space integration is required for the accurate determination of chemical potentials as function of charge concentration. Radiative recombination is calculated according to the van Roosbroeck–Shockley (VRS) formulation,[76] while photocurrent *vs.* voltage calculations follow the SQ approach;[77] formulation and technicalities of these methods are described in detail in ref. 78 and 79.

Thin films of $FASnI_3$ were fabricated as reported in ref. 48 and deposited on quartz substrates. The temperature dependent absorbance was measured by mounting the sample in a cryostat (Oxford Optistat CF) and by illuminating the films with a tungsten light bulb. Transmitted light was detected with an InGaAs detector from Andor (iDus1.7 μm).

3. Results

Structures

Since our goal is a detailed comparative analysis of tin- and lead-halide orbital chemistry and electronic structure, it is appropriate to focus on structural phases not too different from each other; to this aim, all the perovskites considered hereafter are in their low-temperature tetragonal structure; specifically, we consider formamidinium tin iodide $FASnI_3$ (hereafter FASI) in the *P4bm* tetragonal structure, which is found stable below 150 K;[72] and methylammonium tin iodide $MASnI_3$ (MASI) in the *I4cm* tetragonal structure reported below 200 K;[80] these low-T structures have the further bonus, from a theoretical simulation viewpoint, of a fully ordered molecular sublattice, whereas the rotationally disordered cubic phases have the severe (and sometimes unnoticed) difficulty to be hardly accessible by static

Table 1 XRD-measured lattice parameters (a, c); calculated band gap (E_G), valence effective masses (m_V), light ($m_{C,l}$) and heavy ($m_{C,h}$) conduction bands, electronic dielectric constant (ε_∞), refractive index (n_r), intrinsic carrier density (n_i), B-factor (B_{rad})

Material	a (Å)	c (Å)	E_G (eV)	m_V	$m_{C,l}$	$m_{C,h}$	ε_∞	n_r	n_i (cm^{-3})	B_{rad} (s^{-1} cm^{-3})
FASI *P4bm*	8.838[a]	12.407[a]	1.362	0.17	0.08	1.17	3.58	1.95	1.5×10^7	0.45×10^{-10}
MASI *I4cm*	8.758[b]	12.429[b]	1.364	0.19	0.08	1.12	3.92	1.98	1.4×10^6	7.2×10^{-9}
MAPI *I4/mcm*	8.83[c]	12.76[c]	1.614	0.21	0.11	1.59	5.03	2.24	3.6×10^4	1.57×10^{-9}

[a] All results are from the present work, except ref. 72. [b] All results are from the present work, except ref. 80. [c] All results are from the present work, except ref. 81

calculations. These stannates are compared with methylammonium lead iodide $MAPbI_3$ (MAPI) in tetragonal *I4/mcm* symmetry, assuming lattice parameters corresponding to $T \sim 180$ K,[81] that is just above the orthorhombic–tetragonal structures, so that it is reasonable to assume static molecular order, with a high structural similarity to the stannates. Table 1 lists the lattice parameters for the perovskites considered in this work; all the examined materials have $\sqrt{2} \times \sqrt{2} \times 2$ symmetry, with 48 atoms in the unit cells. The relaxed structures for the stannates are reported in Fig. S1.† Upon relaxation, we find the octahedra tilted according to pattern $a^0a^0c^-$, in Glazer notation; average tilting angles are 164°, 160°, and 152° for FASI, MASI, and MAPI, respectively, and average Sn–I or Pb–I atomic distances of 3.124 Å, 3.133 Å, and 3.185 Å, respectively. These structural differences are instrumental to determine different Sn–I and Pb–I bonding strength, and in turn, visibly different electronic and optical properties, as illustrated in the next section.

Electronic and optical properties

In Fig. 1 the calculated band energies and density of states (DOS) for FASI, MASI, and MAPI are shown, all within their respective tetragonal structures, and all without SOC, for consistency. The two stannates display almost identical direct band gap at the Γ point, differing by just 2 meV (Table 1); our calculated $E_G = 1.36$ eV is in good agreement with values extracted from absorption (~1.3–1.4 eV) and photoluminescence (1.2–1.3 eV).[32–37] Our value is also consistent with the $E_G \sim 1.25$ eV obtained for *P4bm* FASI by DFT-1/2 but including SOC,[72] while the heavy demanding GW approach for MASI obtains 1.55 eV and 1.10 eV without and with SOC, respectively.[64] On the other hand, standard DFT gives a largely underestimated $E_G = 0.55$ eV (see Fig. S2†), while for MAPI our DFT calculation gives $E_G = 1.61$ eV, which agrees quite well with the experiment for the reasons discussed in Section 2.

For what concerns the orbital chemistry, the conduction band bottom (CBB) for stannates consists almost exclusively of Sn 5p states, in analogy with the CBB of MAPI, which is made of Pb 6p orbitals. We can notice, however, that FASI displays an additional strong feature not present in the MA-based perovskites, *i.e.* a flat band running 0.7 eV above the CBB across the Brillouin zone (BZ), corresponding to a highly localized FA molecular state; according to the analysis reported in Fig. S3,† the contribution of this flat state to interband absorption is weak, due to the small overlap with the Sn 5s valence band orbitals. Thus, for carriers excited to this state we may expect long recombination lifetimes and slow thermalization, functional to the slow carrier cooling reported for FASI.[35,37]

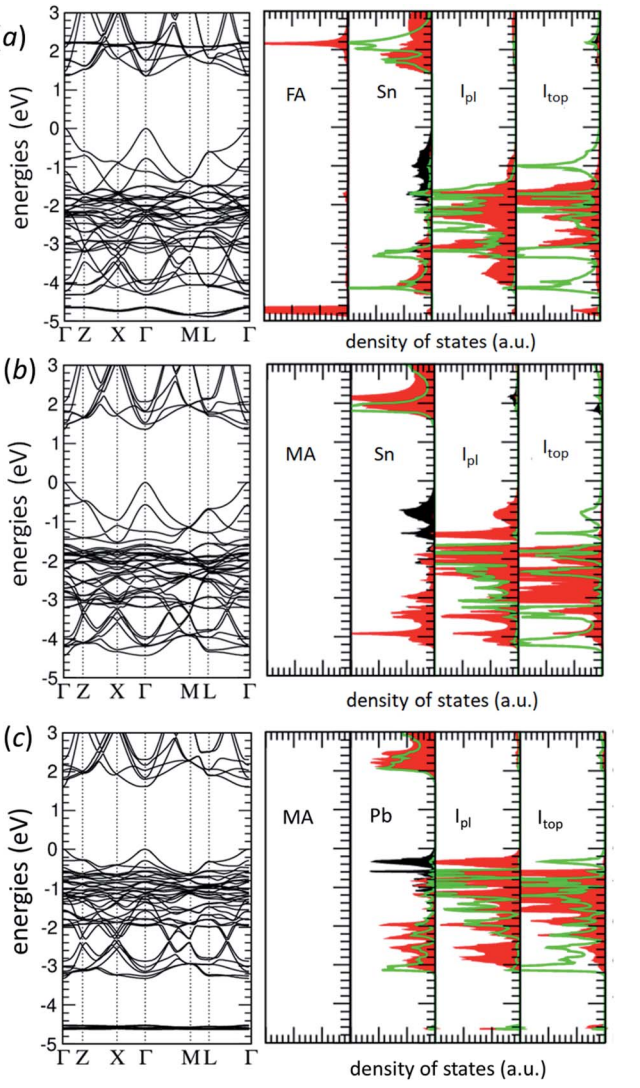

Fig. 1 Calculated band energies and DOS for FASI (a), MASI (b), and MAPI (c). The DOS is separated in atom-specific panels, indicated by labels. Notice that there are 2 types of iodine: those in-plane with Sn or Pb cations (I_{pl}), and those on-top of them (I_{top}). Different colors correspond to different orbital contributions: black for s states, red for p_x, p_y states, green for p_z states; for I_{pl} p_x and p_y are ligand orbitals, so maximally hybridized with Sn 5s or Pb 6s states, while p_z is orthogonal; *vice versa*, for I_{top} p_z is the ligand orbital, and p_x, p_y the orthogonal orbitals.

Another aspect peculiar to the FA sublattice is the orbital ordering induced at the CBB: focusing on the Γ–L and Γ–Z directions, corresponding to the orientation of the cubic axes, we see that in FASI the Sn 5p orbitals split in an energy lower (p_x, p_y) doublet and a higher p_z singlet, with spitting energy of 117 meV; in MASI and MAPI the ordering is reversed: the p_z singlet is more stable than the (p_x, p_y) doublet by 172 meV and 180 meV, respectively; this orbital inversion has an impact on the electron mobility, and it is remarkable that this is caused by the difference in FA and MA coupling with the inorganic sublattice.

For what concerns the valence bands, from the DOS analysis we see that in stannates they are dominated by Sn 5s states, which spread about 2 eV below the valence band top (VBT), while the I 5p states appear ~0.6 eV below the VBT. The difference between stannates and MAPI is apparent in the DOS: the sp valence bandwidth spreads by ~4 eV in stannates and only by 3.2 eV in the lead halide. This signals a stronger Sn 5s–I 5p hybridization with respect to the corresponding Pb 6s–I 5p; notice also the much higher Pb 6s–I 5p DOS peak at the VBT, which indicates smaller orbital overlap in space. In fact, hybridization primarily depends on orbital overlaps and, in turn, atomic distances and tilting angles. In the present case, the atomic radii of Sn 5s and Pb 6s orbitals are similar (2.21 Å and 2.18 Å, respectively); nevertheless, stannates have smaller average Sn–I bond distances, and smaller octahedral tilting, as described in the previous section, thus stronger sp overlaps. To prove this argument, we also calculated the Crystal Orbital Overlap Population (COOP) and the Crystal Orbital Hamiltonian population (COHP) population associated to the Sn 5s–I 5p, and Pb 6s–I 5p bonds (Fig. S4†). We found than in all the examined perovskites, these bonds have a strong bonding character, but for stannates, COOP and COHP have a wider extension in energy and, more importantly, a larger integrated value; indeed we obtain an integrated COHP equal to −0.38, −0.30, and −0.27 eV per bond for FASI, MASI, and MAPI, respectively.

The calculated effective masses are reported in Table 1; for stannates, in particular, the lightest masses are found of the order of 0.1–0.2 electronic masses, consistent with previous results;[64,72] however, at the CBB we obtain a remarkable anisotropy, which results in an electron mobility higher in the (a, b) plane for FASI, and higher along the c axis for MASI and MAPI. Assuming for all the materials the relaxation time $\tau_{rel} \sim 9$ fs calculated for MAPI at room-T,[82] the Drude estimate gives a hole mobility $\mu_h \sim$ 75–95 cm^2 V^{-1} s^{-1} for the 3 perovskites, and 3-D averaged electron mobilities $\mu_e = 138$ cm^2 V^{-1} s^{-1}, 76 cm^2 V^{-1} s^{-1}, and 55 cm^2 V^{-1} s^{-1}, for FASI, MASI, and MAPI, respectively; those are remarkable mobilities, in line with inorganic semiconductors. Despite the simplicity of the estimate, these values are consistent with the measurements reported in literature for hybrid perovskites;[83–89] in particular, in ref. 36 optical pump spectroscopy is used to obtain, for 10%-SnF_2 doped FASI, a mobility ~100 cm^2 V^{-1} s^{-1} which is within our electron–hole mobility range. According to the theoretical analysis carried out in ref. 82, at room temperature and low doping, the electron mobility for lead-halide perovskites is primarily limited by electron-polar optical phonon scattering, coherently with the arguments of ref. 36.

In Fig. 2 we display our calculated and measured absorption spectra *vs.* energy for stannates and MAPI; for clarity, all the curves refer to the 3D average; also, all the curves adopt the same technicalities: below the band gap, absorption is modeled by an exponential Urbach tail with Urbach energy $U = 15$ meV, which is usually observed for lead-halides;[89] furthermore, excitonic contribution is excluded in all the cases. We see some differences in the absorption cross section of the three perovskites, which are especially important at the onset. To better appreciate this aspect, in Fig. 2b zero energy is rescaled to their respective band gap values; we obtain that MAPI has the strongest absorption at the onset, followed by FASI and then MASI. Stronger absorption can be traced back to the peaked DOS near the band extrema, observed for MAPI in Fig. 2b; ultimately, we can give evidence that the differences in absorption primarily derive from structural features, and to a lesser extent from the orbital chemistry of Sn and Pb; to test this scenario, we recalculated the absorption in MAPI by

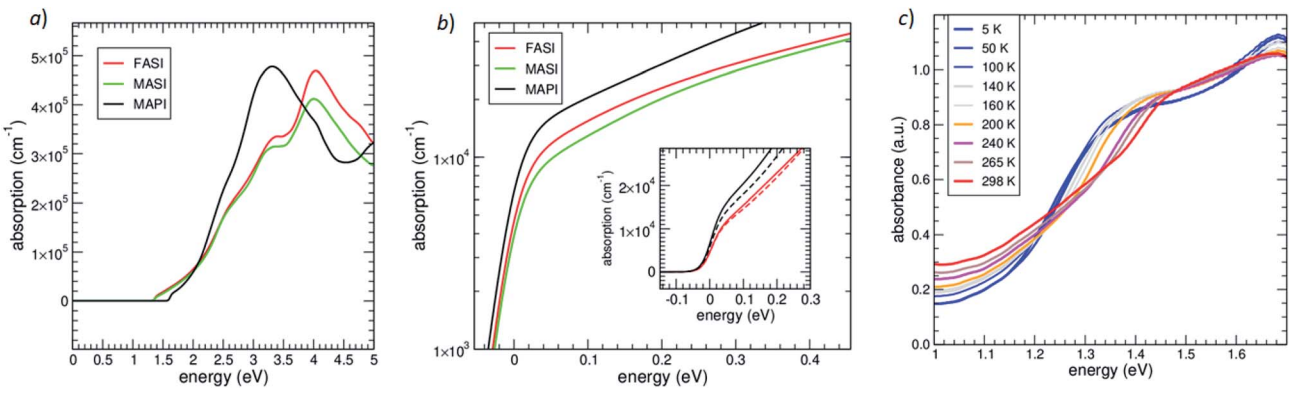

Fig. 2 Calculated absorption spectra for the examined perovskites. (a) Absorption coefficient *vs.* energy; (b) absorption on a logarithmic scale with the respective band gap values rescaled to zero, in order to put in evidence the different absorption at the onset; inset: enlargement in a small interval around the onset; the black dashed line is for a fake material with MAPI atomic structure but with Pb replaced by Sn, the red dashed line for a fake material with FASI atomic structure and Sn replaced by Pb (see text). (c) Measured absorbance for FASI from low to high temperature; absorbance is filtered out above 1.7 eV.

keeping the atomic structure frozen, and fully replacing Pb with Sn (black dashed curve, inset of Fig. 2b): we see that the purely chemical substitution only marginally changes the MAPI absorption; similarly for FASI, we kept the atomic structure frozen, and substituted Sn with Pb (red dashed curve, inset of Fig. 2b): again, the absorption is marginally changed; the conclusion is that structural differences, and specifically, octahedral rotations, play the major role in the larger absorption of plumbates at the onset. Remarkably, the same holds for the band gap: the frozen-atom Pb to Sn substitution changes the MAPI band gap from 1.61 eV to 1.77 eV, while the Sn to Pb substitution at frozen FASI structure changes the FASI band gap from 1.36 eV to 1.27 eV. We can conclude that the larger band gap of lead perovskites ultimately derives from larger octahedral tilting, in turn causing smaller Pb 5s–I 5p hybridization, and correspondingly smaller valence bandwidth than in stannates. In Table 1 we also report our calculated electronic dielectric constants (ε_∞) and refraction indices (n_r); for the two stannates these values are rather similar, while MAPI displays larger electronic screening and slower light transmission than the Sn-based perovskites.

In Fig. 2c we report the measured absorbance for FASI in a temperature range from low to room T. We clearly see the absence of any excitonic contribution, even at low temperature, in agreement with previous reports; the optical band gap obtained by Tauc plot is 1.34 eV at room-T, and ~0.1 eV lower at low-T; these values are in satisfying agreement with our theoretical band gap of 1.36 eV, which is formally calculated at $T = 0$. We also notice that a substantial spectral weight is present below the band gap, which adds up to the intrinsic inter-band transitions. This extrinsic below-gap absorption is not surprising, as it likely derives by intra-gap defects typically observed for stannates.[32–35] In ref. 54 it is discussed that this smeared out onset transfers into a photoluminescence linewidth much larger than for Pb-based compounds, and depends on the material quality. A direct comparison of calculated and measured absorption is complicated by several aspects which are difficult to be accurately matched, such as temperature, sample thickness, and, most of all, the extrinsic factors which generate below band gap absorption; an easier connection between experiment and theory can be established at level of radiative recombination rate, as structural disorder and native doping can be included, albeit with some approximations, in the simulations.

Photoluminescence spectra

Photoluminescence (PL) is a key aspect to evaluate whether materials are viable for optoelectronic applications. From a theoretical viewpoint, the photoluminescence spectra PL(ε), where ε is the photon energy, can be calculated in quasi-equilibrium conditions at varying carrier population by exploiting the VRS approach.[76] As the injected electron–hole population can be traced back to the laser pulse fluence, the calculated PL can be directly connected to the photoluminescence measured in pump and probe experiments, thus furnishing a significant term of comparison to the experimental analysis. In Fig. 3a and b we display the calculated spectra for FASI at room T, renormalized to the peak values; different lines refer to different $n = p$ injected populations, considered in the interval from $n = 10^{14}$ cm^{-3} up to 5×10^{19} cm^{-3}. In Fig. 3c and d the same curves are reported for a lower $T = 24$ K; we remark that temperature is accounted for only in terms of Fermi–Dirac

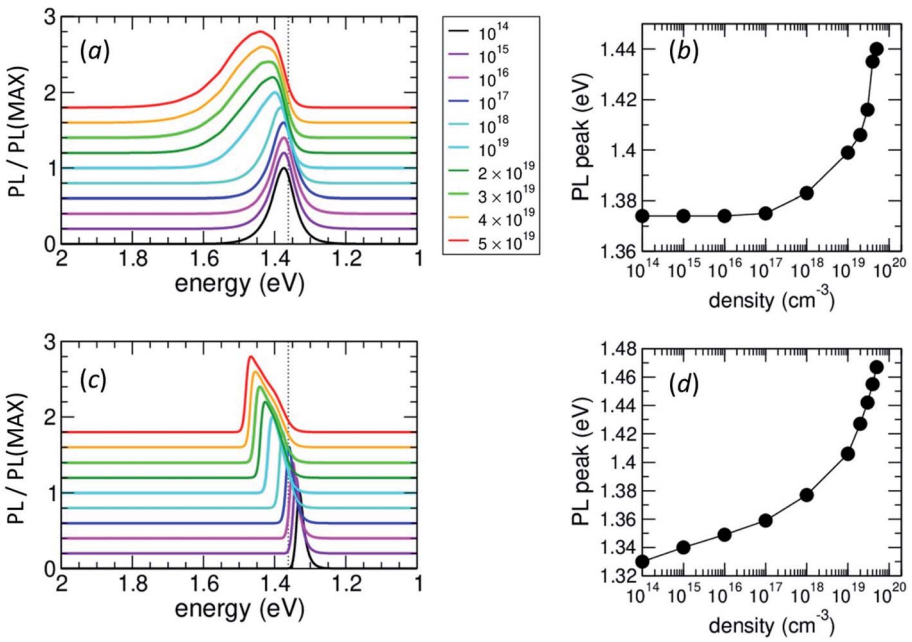

Fig. 3 (a) Calculated PL spectra *vs.* photon energy for FASI at room T, renormalized to the PL maximum value; curves of different colors refer to the carrier densities n reported in the legend; the dotted line indicates the band gap. (b) PL peak energy *vs.* n at room T. (c) and (d) Same as (a) and (b) but for $T = 24$ K, respectively.

occupancies and quasi Fermi-levels, whereas the electronic structure refers to the *P*4*bm* tetragonal phase.

At room-*T*, Fig. 3a, the PL curves remain substantially unchanged with n up to $n \sim 10^{17}$ cm^{-3}, while above this value a remarkable blue shift is apparent, together with a clear PL width enlargement; in Fig. 3b the peak energy is plotted as a function of n; the peak is constant up to $n \sim 10^{17}$ cm^{-3}, then it rises by 0.07 eV at $n = 5 \times 10^{19}$ cm^{-3}; at low-*T* the peak *vs.* charge density curve is qualitatively different: the peak energy changes linearly with n up to $n \sim 10^{17}$ cm^{-3}, then it rises steeply, increasing by 0.15 eV across the whole n range; this is understandable, since at low temperature the e–h chemical potential is already quite high and close to the band gap at $n \sim 10^{14}$ cm^{-3}, thus band filling effect shows up much in advance than at room *T*. The blue shift described by our calculations is in good qualitative and partially quantitative agreement with the experimental findings of ref. 35; however, in the experiment it is evidenced that this blue shift also comes from hot, unthermalized carrier recombination, while the theoretical description assumes thermalization, so it only captures band-filling effects.

Integrated photoluminescence

In Fig. 4 we display the energy-integrated photoluminescence, *i.e.* the radiative recombination rate, for the perovskites at varying injected charge n, calculated for $T = 300$ K. To understand the photoluminescence behavior, it is essential to visualize (Fig. 4a) how the e–h chemical potential μ_{eh} changes with n: at low n, μ_{eh} rises logarithmically with n, the intercept with the band gap value (indicated by dashed horizontal lines) defining the inversion population n_{inv} for each perovskite (dotted vertical lines of corresponding color). We obtain $n_{inv} = 3.1 \times 10^{18}$ cm^{-3} for FASI, 3.5×10^{17} cm^{-3} for MASI, and 1.5×10^{18} cm^{-3} for MAPI. It is remarkable that the two stannates, while having almost identical band gap, differ in n_{inv} by about an order of magnitude; in fact, for a given n, μ_{eh} is ~100 meV higher in MASI than in FASI; this is due to the lower absorption cross section at the onset for the former, causing the shift of quasi Fermi levels towards the corresponding band extrema. Another consequence of the lower absorption is the one-order-of-magnitude lower intrinsic carrier concentration n_i at room-*T* for MASI, reported in Table 1. On the other hand, MAPI has its chemical potential $\mu_{eh} \sim 300$ meV higher than FASI due to the larger band gap, and correspondingly, n_i which is 3 orders of magnitude smaller than FASI.

The difference in chemical potentials crucially reverses on the radiative recombination rate R (number of emitted photons per unite time and volume); let us first analyze the solid lines of Fig. 4b, derived assuming a moderate Urbach energy of 15 meV for all the perovskites. Notice that R depends linearly on the absorption cross section $a(\varepsilon)$, and exponentially on $-(\varepsilon - \mu_{eh})/k_BT$ (see *e.g.* ref. 79). At the onset, the dominant factor is the exponential decay governed by $\Delta E = (E_g - \mu_{eh})$; for example, at $n = 10^{15}$ cm^{-3} we have $\Delta E = 0.32$ eV, 0.39 eV, and 0.43 eV, for MASI, MAPI, and FASI, respectively; these values translate into $R = 7 \times 10^{21}$ s^{-1} cm^{-3} for MASI, 1.3×10^{21} s^{-1} cm^{-3} for MAPI, 4×10^{19} s^{-1} cm^{-3} for FASI.

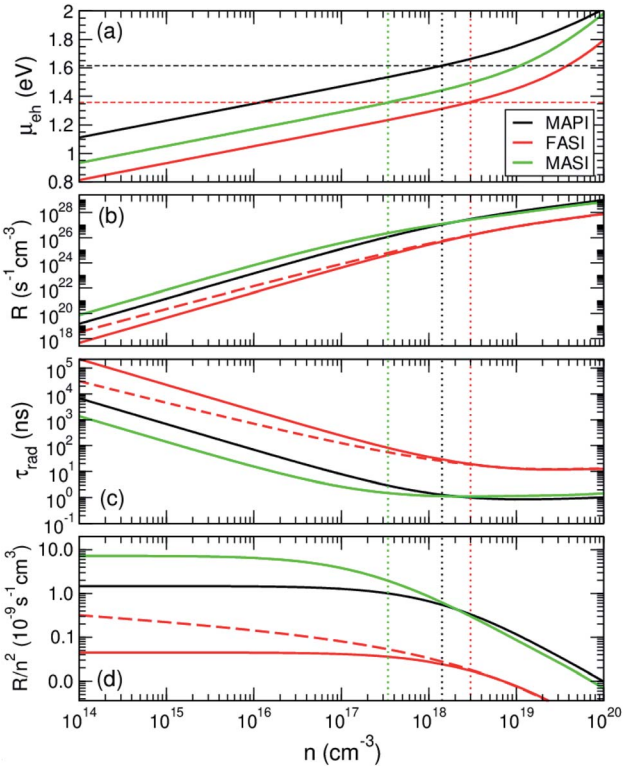

Fig. 4 (a) Electron–hole chemical potential as a function of injected carrier concentration, for the 3 perovskites indicated in the legend; horizontal dashed and vertical dotted lines indicate band gap and population inversion threshold for the perovskite of corresponding color. (b) Radiative recombination rate for the 3 perovskites; the solid curves are calculated assuming an Urbach energy $U = 15$ meV; only for FASI, the recombination rate is also calculated for $U = 32$ meV (red dashed line). (c) n/R corresponds in the linear regime to the radiative recombination time t_{rad}; solid and red dashed lines are the FASI values for $U = 15$ meV and 32 meV, respectively (d) R/n^2 corresponds in constant regime to the radiative bimolecular recombination factor; solid and red dashed lines for FASI are the same as in (b) and (c).

Rather than to R, it is customary in literature to refer to the linear and quadratic coefficients, related to the radiative recombination lifetime τ_{rad} and the bimolecular recombination factor B, respectively. In the case of purely quadratic R behavior, we can calculate these coefficients as $\tau_{rad} = n/R$ (Fig. 4c) and $B = R/n^2$ (Fig. 4d). The low-n interval where n/R and R/n^2 are linear and constant with n, respectively, defines the limit of the purely quadratic regime. From our results, we see that this limit is remarkably material dependent: for FASI and MAPI, quadraticity is conserved up to $n \sim 10^{17}$ cm^{-3}; beyond this threshold, R/n^2 decrease and n/R saturates to a constant value. For MASI, on the other hand, deviation from the quadratic behavior is already visible at $n \sim 10^{16}$ cm^{-3}. This deviation, commonly denoted as band filling effect, signals an increasing asymmetry of spectral weight at VBT and CBB, which derives from the detail of the band energies. For hybrid perovskites the different orbital character and ordering which characterize CBB and VBT results in substantial deviation from the quadratic behavior even at low charge density. This aspect is sometime overlooked in analysis based on the photoluminescence measured across a large

charge injection range, in which the emission intensity is exclusively associated to the quadratic behavior. In Fig. S5† a detailed analysis is shown where $R(n)$ for FASI is separately analyzed in different density ranges.

From our results we obtain $B = 7.6 \times 10^{-9}$ s^{-1} cm^3 (MASI), 1.45×10^{-9} s^{-1} cm^3 (MAPI), 0.4×10^{-10} s^{-1} cm^3 (FASI). For MASI and MAPI these values are well within the ballpark of the reported measurements.[22–26,85] For FASI, on the other hand, our calculated value is at the lower bound estimate of the reported experimental range (*e.g.* 3.4×10^{-9} s^{-1} cm^3 according to ref. 35, 4×10^{-9} s^{-1} cm^3 for ref. 32, 0.7×10^{-10} s^{-1} cm^3 for ref. 36), but in perfect agreement with a previous LDA-1/2 calculation;[72] this suggests that the theoretical estimate is solid, and the discrepancy with the experiment should be sought for in the high sensitivity of radiative recombination to extrinsic factors, such as native doping and structural disorder. An indication consistent with this scenario is the large Urbach $U = 32$ meV estimated in ref. 35 for FASI, which is about the double of what is typically reported for MAPI.[89] It turns out that, by recalculating R with $U = 32$ meV for FASI (red dashed line), we obtain $B \sim 3 \times 10^{-10}$ s^{-1} cm^3, that is about an order of magnitude bigger, and much closer to the experimental estimates. Moreover, Fig. 4d shows that such a big U largely distorts the ideal quadratic behavior at low n; the influence of the Urbach tail progressively fades at growing n, but it remains visible up to $\sim 10^{18}$ cm^{-3}. Without pretense of being predictive, the simple Urbach modeling has the merit to put in evidence how radiative recombination is crucially dependent on the detail of the electronic energies in the vicinity of the band gap, and that order of magnitude differences in the recombination rate can easily spur from in-gap DOS tail produced by structural and chemical disorder, motivating the typically large spread of values reported in literature for the same material.

Hole doping and Burstein–Moss effect

At the experimental level, a marked difference is reported for the radiative recombination rate of FASI and MAPI: the former is found to behave linearly in n even at low concentration,[33–36] while in MAPI it is found quadratic up to about 10^{18} cm^{-3}.[22] As the excitonic contribution is ruled out, the linear behavior of FASI is explained as due to the radiative recombination between electrons and defect-induced holes, in the hypothesis that the acceptor concentration is much larger than photo-injected carrier populations. According to our results, this defect concentration should be not less than $\sim 10^{17}$ cm^{-3} for FASI, and not less than 10^{16} cm^{-3} for MASI, since for lower n the intrinsic radiative recombination is quadratic. Consistently, several experiments estimate in no less than 5×10^{17} cm^{-3} the amount of native holes present in the stannates.[33–36] Since the recombination probability depends on the product of electron and hole charge densities in the sample, the presence of native holes greatly enhances the recombination obtained for a given charge injection, thus causing in FASI the occurrence of an amplified spontaneous emission at low injection threshold,[33] which can be conveniently exploited in lasing application.

The effect of hole doping in the recombination process is usually modelled by a linear (*i.e.* monomolecular) term, as $R = Bn(p + p_0)$, where p_0 is the hole doping concentration, and $n = p$ the injected charge. In our VRS approach,[76] p_0 is included at a more fundamental level in the band occupancy, and in turn, in the chemical potential. In Fig. 5 we remap the radiative recombination properties for FASI with the inclusion of a variable amount of hole doping concentration, from $p_0 = 10^{14}$ cm^{-3} to $p_0 = 5 \times 10^{19}$ cm^{-3}.

Starting the analysis from the chemical potential (Fig. 5a and b), we see that the inclusion of p_0 increases μ_{eh}, which now follows the logarithmic behavior $(\mu_{eh} - E_g)/K_BT \sim \ln(np + np_0)$, see the inset of Fig. 5a on a linear scale. The most interesting aspect occurs when p_0 approaches n_{inv}: we see that for $p_0 \sim 10^{18}$ cm^{-3} (red solid line) and beyond, the doping concentration is large enough to shift the chemical potential well above the band gap, thus resulting in a band gap enhancement due to doping. This effect, called Burstein–Moss, implies an increase of the optical threshold under charge injection by a quantity $\Delta E_{BM} = \mu_{eh} - E_g$, and it is known to occur in stannates, furnishing a direct proof to the presence of a large hole doping concentration.[32–37] According to our results, $\Delta E_{BM} = 10$ meV for $p_0 = 10^{18}$ cm^{-3} and 78 meV for $p_0 = 10^{19}$ cm^{-3}. Another way to describe this effect is considering the intercept of μ_{eh} with E_g occurring at lower charge injection, *i.e.* n_{inv} is progressively reduced by the increase of p_0. For example, our results indicate that for $p_0 = 10^{19}$ cm^{-3}, population inversion should occur for an injected charge density as low as $n = 3 \times 10^{17}$ cm^{-3}.

In Fig. 7c and d the recombination rate is plotted for the same hole doping values; as p_0 increases, we see the progressive change of $R(n)$ from quadratic to linear regime, which sets in for $p_0 > n$. Interestingly, when n approaches n_{inv}, R reaches a saturation value which is independent on p_0; this can be better appreciated in Fig. 5d where R is plotted as a function of p_0, for fixed n values: at large p_0, R becomes doping-independent, irrespectively of n. The ratio of this behavior is that electron–hole recombination rate cannot increase indefinitely if the two carrier types do not both increase; in other words, beyond a certain p_0 the electrons all recombine so quickly that R cannot increase further. This saturation regime is not described by the simple Bnp_0 linear term; in fact, we obtain that a satisfying description of R is given by the following expression:

$$R = \frac{B(n^2 + np_0)}{1 + \frac{n}{n_{inv}} + \frac{p_0}{n_{inv}}} = \frac{Bnn_{inv}}{1 + \frac{n_{inv}}{n + p_0}} \quad (1)$$

which is only based on two parameters, B and n_{inv}; in Fig. 5c and d we see that the results of this model (open squared symbols) quite satisfyingly interpolate the VRS values (solid lines of corresponding color) across the whole examined range as a function of both n and p_0. From eqn (1) we obtain that for either n or p_0 sufficiently larger than n_{inv}, the radiative rate reaches the saturation value $R \sim Bnn_{inv}$.

For what concern the radiative lifetime (Fig. 5e and f), the inclusion of doping changes the behavior from linear to constant with n; according to eqn (1), it can be modeled as:

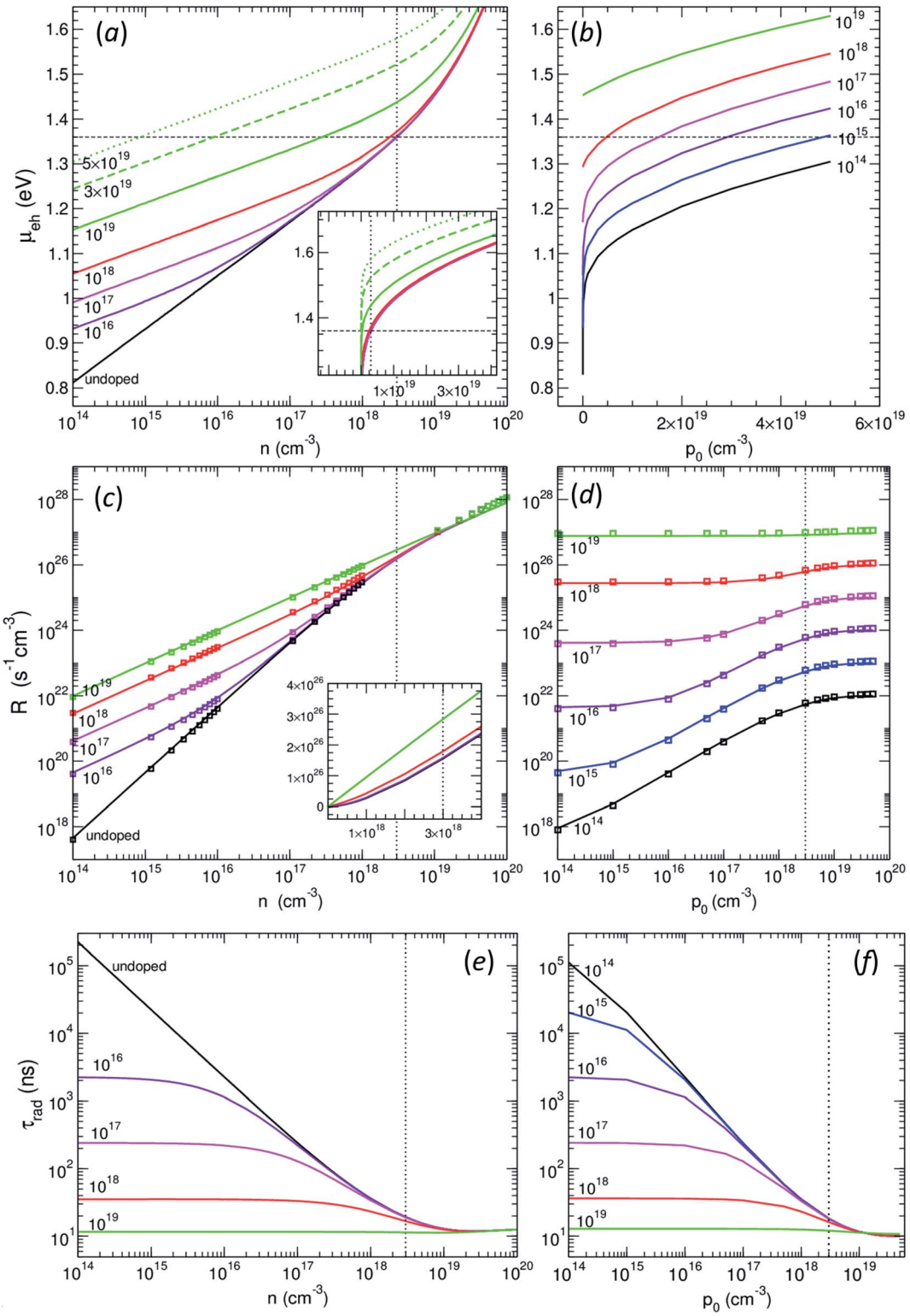

Fig. 5 Calculated radiative recombination properties as a function of injected carrier concentration $n = p$ and hole doping concentration p_0 for FASI. In all the panels horizontal and vertical lines indicate FASI band gap and inversion population threshold, respectively. (a) e–h chemical potential *vs.* n; the colored lines refer to different p_0 values, indicated in figure. (b) Chemical potential *vs.* p_0; the colored lines refer to different n values, indicated in figure. (c) Radiative recombination rate *vs.* n for different p_0. (d) Radiative recombination rate *vs.* p_0 for different n. Open squared symbols are model values calculated from eqn (1). (e) Radiative lifetime *vs.* n for different p_0 (f) radiative lifetime *vs.* p_0 for different n.

$$\tau_{rad} = \frac{n}{R} = \frac{1}{Bn_{inv}}\left(1 + \frac{n_{inv}}{n + p_0}\right) \quad (2)$$

For p_0 larger than n but still much smaller than n_{inv}, we obtain $\tau_{rad} \sim 1/Bp_0$; so τ_{rad} is constant with n and inversely proportional to p_0; for $p_0 = 5 \times 10^{17}$ cm^{-3}, which is the value estimated in stannates, we obtain $\tau_{rad} = 50$ ns for $U = 15$ meV, and 6.7 ns for $U = 32$ meV. In the saturation regime, for p_0 much larger than n_{inv}, the relaxation time reaches the doping-independent, lower limit value $\tau_{rad} = 1/Bn_{inv}$, equal to 8.3 ns for $U = 15$ meV, and 1.1 ns for $U = 32$ meV; this corresponds to the smaller recombination lifetime that can be reached in a given material in absence of non-radiative events, *i.e.* the minimal time required for an electron–hole couple to recombine radiatively, irrespective of how many electron–hole couples are present in the system. Our calculated lifetime for FASI is in the range of the values reported in literature (~1–10 ns), extracted from PL measurements.[32–36,48,54] However, we should take in mind that this is only the radiative contribution, estimated to be about 10% of the total monomolecular value for stannates;[35–37] so, the vast majority of recombination events, which are largely responsible of the unsatisfying efficiency of stannates, has a non-radiative origin, and is likely associated to hole-trapping.

Localized holes

Including non-radiative hole trapping effects in the *ab initio* description is an overwhelming achievement which outpours the limits of present computational capabilities; in order to furnish some hints at qualitative level on the radical disruption that localized holes can produce into the electronic properties of the stannates, we took advantage of the capabilities of the VPSIC approach to describe the presence of a substitutional Sn^{4+} ion in tetragonal FASI; the corresponding band structure is reported in Fig. 6. We can see (in red) a double-degenerate hole band derived by the empty 5s states of the Sn^{4+} ion running through the whole BZ, visibly separated by the filled band manifold of the 5s Sn^{2+} ions, and spanning an energy interval of about 1 eV above the VBT. This electronic configuration was achieved by subtracting 2 electrons from the simulation cell and applying a penalty function on one of the Sn 5s states in order to induce its charge depletion (in plane waves basis implementation charge neutrality is restored by an homogeneous compensating background). The hole band runs ~0.5 eV above the VBT, and ~0.8 eV below the CBB, on average over the BZ; specifically, at Γ the hole band is 0.36 eV below the CBB and 0.88 eV above the VBT. We remark that, while the hole band dispersion would be progressively reduced in the localized-charge limit (that is describing the hole in larger and larger simulation cells), its average energy position (indicated by the dashed red line) is likely correct even for realistic hole doping concentrations, thus we can consider this as a reliable energy prediction for the holes induced by Sn^{2+} to Sn^{4+} substitutions. Clearly a large amount of such a near mid-gap energies could easily disrupt the intrinsic behavior of the stannates.

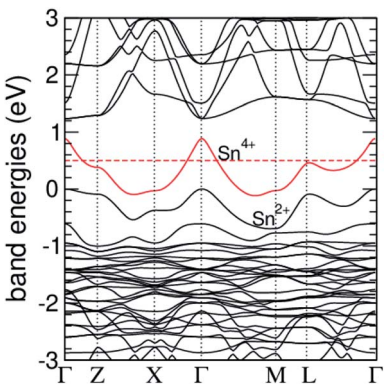

Fig. 6 Band structure for tetragonal MAPI, with one Sn^{2+} to Sn^{4+} substitution; the red band is the empty, double-degenerate hole band derived from the Sn^{4+} 5s orbital. Red dashed line indicates the hole band center, which gives an estimate of the trapping-hole energy in the spatial localized limit.

Photoconversion properties

In this section we extend the comparison of stannates and plumbates to photocurrent *vs.* potential properties, calculated according to SQ.[77] In Fig. 7 we show the calculated short-circuit current density J_{sc}, output current density J, and output power density P_{out} *vs.* voltage for FASI and MAPI; since in all calculations we use the AM1.5G solar spectrum whose input power density is 100 mW cm^{-2}, P_{out} also coincides with the calculated power conversion efficiency (PCE) in percent. Two sets of data are shown for each perovskite, one for an absorber thickness of $L = 100$ nm, and the other for a very thick sample to represent a condition of full absorption, *i.e.* the ideal SQ limit. To compare the perovskites at the purely intrinsic level, the Urbach effect is not included here, but separately evaluated at the end.

According to the band gap difference, we expect FASI to display visibly larger J_{sc} and smaller open-circuit voltage (V_{oc}) than MAPI; however, for $L = 100$ nm the higher MAPI absorption at the onset partially compensates the larger band gap, so that J_{sc} for MAPI is only slight smaller than for FASI, resulting in a slightly larger PCE (16.5% for MAPI against 15.5% for FASI); in the SQ limit the situation is reversed: the difference in absorption fades out, and J_{sc} becomes sensitively larger for FASI.

To better evaluate the effect of thickness, in Fig. 8 we plot J_{sc}, V_{oc} and PCE at varying L for the 3 perovskites. The curves for the two stannates substantially overlap, due to the similar band gap; for what concerns MAPI, J_{sc} matches the values of tin halides up to $L \sim 100$ nm due to the compensation between band gap and absorption rate; above this thickness, the difference in absorption is less and less significant, so J_{sc} becomes increasingly larger for tin halides; in the limit of full absorption we find $J_{sc} = 34.2$ mA cm^{-2} and 28.5 mA cm^{-2} for stannates and MAPI, respectively; on the other hand, V_{oc} decreases by about 6% across the whole L range, as a consequence of the increasing recombination current which depends linearly on the absorption probability; we also see that the voltage difference between tin and lead halides ($\Delta V_{oc} \sim 0.13$ eV) is little sensitive to L.

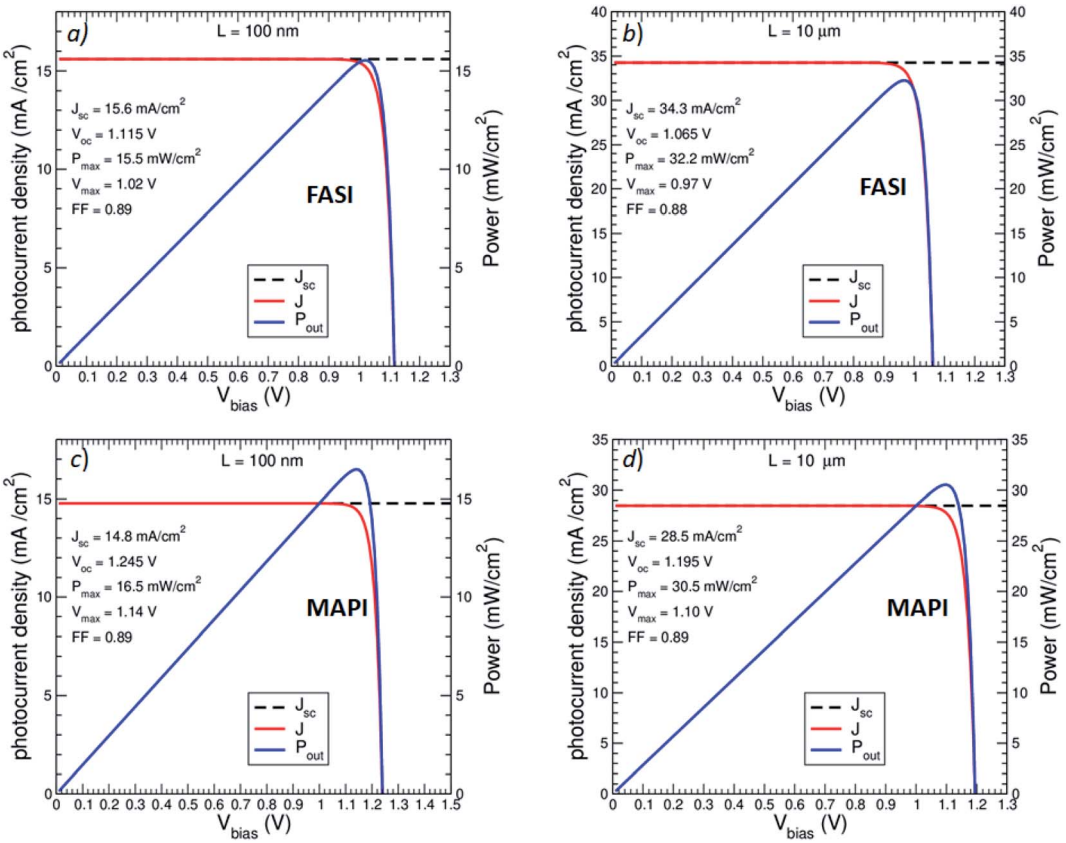

Fig. 7 Calculated current and power density *vs.* potential curves for tetragonal FASI and MAPI, for two different thicknesses, as indicated by the label in figure. Each panel shows the short-circuit current density J_{sc}, total current density J, and output power density P_{out}; open-circuit potential V_{oc}, maximum output power density P_{max}, maximum potential V_{max}, and fill factor FF are also indicated in the figure for each calculation. All calculations assume AM1.5G Sun spectrum, with input power density 100 mW cm^{-2}, so P_{out} corresponds to the power conversion efficiency value (%).

Remarkably, ΔV_{oc} is much smaller than their band gap difference ($\Delta E_g = 0.25$ eV); in the large-L limit, the potential loss $E_g - V_{oc}$ is 0.42 eV for MAPI, and only 0.30 eV for FASI and MASI, as a consequence of the smaller band gap which is so close to the optimal SQ value. The combination of current and potential behavior makes the output power (Fig. 8c) about 10% higher for

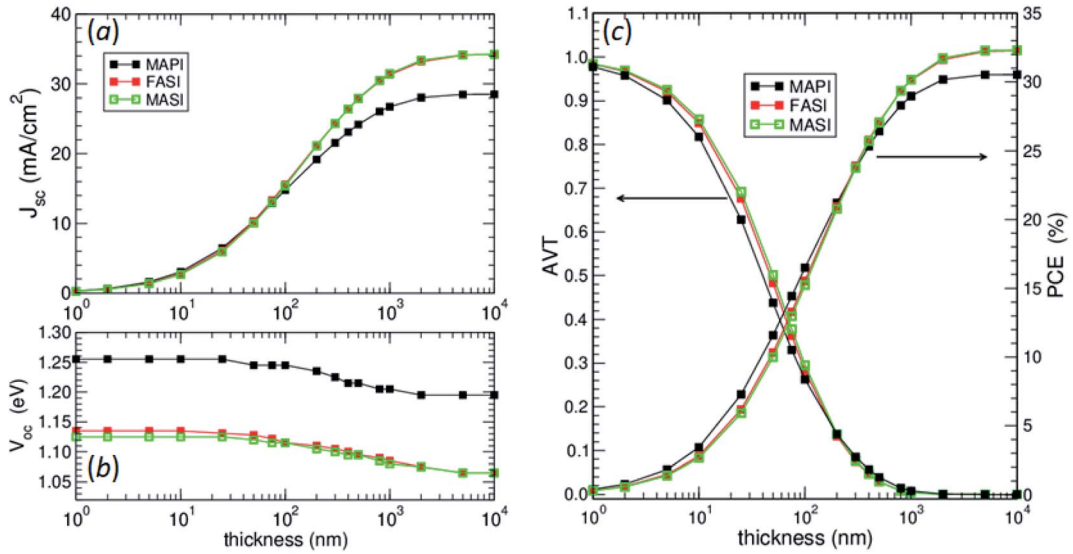

Fig. 8 (a) Calculated short-circuit currents for the 3 examined perovskites as a function of the absorber thickness. (b) Open-circuit potentials. (c) Power conversion efficiency (PCE) and average visible transparency (AVT).

MAPI up to $L \sim 300$ nm due to the larger V_{oc}, then higher for stannates at larger thickness, as the larger current of stannates overcompensates the difference in V_{oc}. At the crossing point $L =$ 300 nm, they all display an ideal PCE ~23.7%, while the large-L efficiency limit gives 30.5% for MAPI and 32.3% for stannates (under AM1.5G illumination). It is important noticing that, according to our analysis, the more favorable band gap energy of the stannates determines an actual advantage over lead halides only for thick absorber layers.

The smaller absorption at the onset suggests that tin halides could be more suited than MAPI for smart window applications, achieving a good compromise between photoconversion and transmission in the visible rage; to the aim, we report in Fig. 8c a back-to-back calculations of PCE and average visible transparency (AVT) *vs.* L for the examined perovskites (AVT is the energy-averaged transmittance $e^{-\alpha L}$ over the visible range); we see that for small thickness the AVT for stannates is visibly larger; for example at $L = 40$ nm, the PCE ~ 11% and the AVT ~ 50%; these are record-high numbers, which classifies stannates at the top of the presently known semi-transparent absorbers.[90–96] Above 200 nm the difference in absorption fades and the AVT for stannates and plumbates becomes the same.

Finally, in Fig. 9 we report calculations for currents, potentials, and PCE at varying Urbach energy for MAPI and FASI (an accurate analysis of Urbach effects in the SQ model can be found in ref. 97). In general, the Urbach tail produces two contrasting effects on J_{sc} and V_{oc}: the former increases slightly and almost linearly, as owed to the enlarged absorption energy region, while the latter decreases due to the growth of recombination rate, previously analyzed in Fig. 4. These two effects nearly compensate up to $U \sim$ 15–20 meV, so the PCE barely changes. Above this threshold, J_{sc} keeps increasing mildly, while V_{oc} severely shrunk, resulting in a rapid decrease of PCE. For the $U \sim 32$ meV reported for MASI we obtain a PCE of 27% at $L = 10$ μm (thus, about 15% lower than the ideal 32.3%), 13.6% at $L = 100$ nm (against the ideal 15.6%), and 22.5% at $L =$ 400 nm (against the ideal 25.3%). According to these results, this large U does not preclude the possibility of stannates to reach quite satisfying PCE, on par with those reached in plumbates. Of course, the presence of non-radiative trapping defects which is the primary cause of inefficiency in stannates is not captured by the Urbach model, and must be treated by more fundamental approaches.

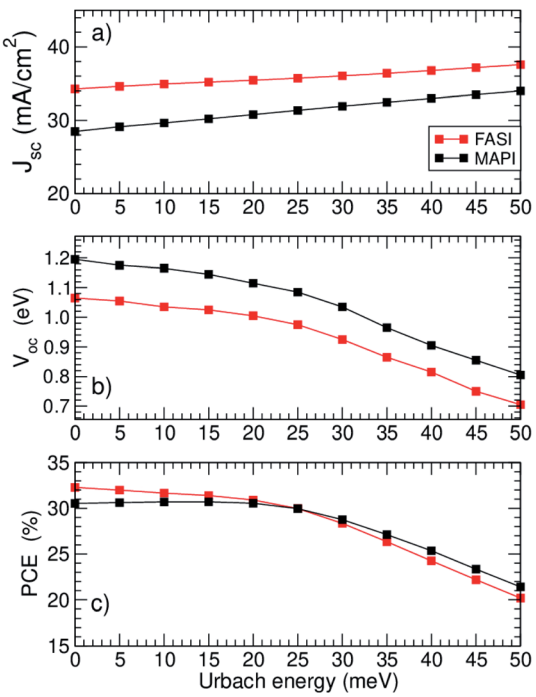

Fig. 9 Calculated photoconversion properties for MAPI and FASI, at varying Urbach energy, for $L = 10$ μm. (a) Short-circuit currents. (b) Open-circuit potentials. (c) Power conversion efficiencies.

4. Conclusions

We used advanced *ab initio* calculations and absorption measurements to achieve a detailed investigation of electronic, optical, and photoconversion properties of Sn-based perovskites, in comparative analysis with the MAPI prototype, with the aim of tracing the intrinsic limit of these materials and their potential use as lead-free absorbers for solar cell and optoelectronic applications. Our results describe several fundamental characteristics, such as the band gap, the orbital chemistry, and the bandwidth of the electronic states primarily involved in the optical transition, unveiling how these aspects are reflected in the recombination and photoluminescence process, and in turn in the photocurrent and power conversion efficiency. The comparison of theory and experiment is complicated by the large defect concentration typically present in stannates; however, properties not directly influenced by defects, such as the fundamental band gap and the blue shift of photoluminescence peak at increasing charge injection, are in good quantitative agreement.

According to our analysis, tin-halides have a lower absorption rate at the onset than lead halides, as a result of larger orbital hybridization of the valence manifold; however, this aspect does not significantly affect the photoconversion capability of stannates: for what concern short-circuit photocurrent, the lower absorption is overcompensated by the smaller band gap; as for the open-circuit potential, the lower band gap of tin-halides generates a potential loss remarkably smaller than for lead halide, thus reducing the open-circuit voltage difference. Overall, we estimate a power conversion efficiency peaking at 32.3% and 30.5% for stannates and MAPI under AM1.5G illumination, respectively; we also predict a remarkably large visible transparency in the small thickness limit for stannates, which makes them potentially interesting for semitransparent solar cells.

Conflicts of interest

The authors declare no competing financial interests

Acknowledgements

Work supported by Fondazione di Sardegna through project 2F20000210007 'Perovskite materials for photovoltaics', and by

project PRIN 2017 "TOPSPIN", funded by Italian Ministry of University. S. K. acknowledges a research fellowship (grant no. 408012143) awarded by the Deutsche Forschungsgemeinschaft (DFG). This work was partially financed through the Materials for Sustainability (Mat4Sus) program (739.017.005) of The Netherlands Organization for Scientific Research (NWO). AM acknowledges Italian MIUR for funding through project PON04a2 00490 "M2M Netergit", CNR for Projects CNR/RFBR (Russia) "BNCT" and Short Term Mobility "HALIDES", and PRACE for awarding access to Marconi KNL at CINECA, Italy, through project "PROVING-IL" (2019204911).

References

1 M. M. Lee, J. Teuscher, T. Miyasaka, T. N. Murakami and H. J. Snaith, Efficient Hybrid Solar Cells Based on Meso-Superstructured Organometal Halide Perovskites, *Science*, 2012, **338**, 643–647.

2 S. D. Stranks, G. E. Eperon, G. Grancini, C. Menelaou, M. J. P. Alcocer, T. Leijtens, L. M. Herz, A. Petrozza and H. J. Snaith, Electron-Hole Diffusion Lengths Exceeding 1 Micrometer in an Organometal Trihalide Perovskite Absorber, *Science*, 2013, **342**, 341–344.

3 G. Xing, N. Mathews, S. Sun, S. S. Lim, Y. M. Lam, M. Grätzel, S. Mhaisalkar and T. C. Sum, Long-Range Balanced Electron- and Hole-Transport Lengths in Organic-Inorganic $CH_3NH_3PbI_3$, *Science*, 2013, **342**, 344–347.

4 J. Burschka, N. Pellet, S.-J. Moon, R. Humphry-Baker, P. Gao, M. K. Nazeeruddin and M. Grätzel, Sequential Deposition as a Route to High-Performance Perovskite-Sensitized Solar Cells, *Nature*, 2013, **499**, 316–319.

5 W. S. Yang, J. H. Noh, N. J. Jeon, Y. C. Kim, S. Ryu, J. Seo and S. Il Seok, High-performance photovoltaic perovskite layers fabricated through intramolecular exchange, *Science*, 2015, **348**, 1234–1237.

6 F. Deschler, M. Price, S. Pathak, L. E. Klintberg, D.-D. Jarausch, R. Higler, S. Hüttner, T. Leijtens, S. D. Stranks, H. J. Snaith, M. Atatüre, R. T. Phillips and R. H. Friend, High Photoluminescence Efficiency and Optically Pumped Lasing in Solution-Processed Mixed Halide Perovskite Semiconductors, *J. Phys. Chem. Lett.*, 2014, **5**, 1421–1426.

7 D. Shi, V. Adinolfi, R. Comin, M. Yuan, E. Alarousu, A. Buin, Y. Chen, S. Hoogland, A. Rothenberger, K. Katsiev, *et al.*, Low Trap-State Density and Long Carrier Diffusion in Organolead Trihalide Perovskite Single Crystals, *Science*, 2015, **347**, 519–522.

8 Q. Dong, Y. Fang, Y. Shao, P. Mulligan, J. Qiu, L. Cao and J. Huang, Electron-Hole Diffusion Lengths >175 μm in Solution-Grown $CH_3NH_3PbI_3$ Single Crystals, *Science*, 2015, **347**, 967–970.

9 T. Leijtens, G. E. Eperon, A. J. Barker, G. Grancini, W. Zhang, J. M. Ball, A. R. S. Kandada, H. J. Snaith and A. Petrozza, Carrier trapping and recombination: the role of defect physics in enhancing the open circuit voltage of metal halide perovskite solar cells, *Energy Environ. Sci.*, 2016, **9**, 3472–3481.

10 H. Oga, A. Saeki, Y. Ogomi, S. Hayase and S. Seki, Improved Understanding of the Electronic and Energetic Landscapes of Perovskite Solar Cells: High Local Charge Carrier Mobility, Reduced Recombination, and Extremely Shallow Traps, *J. Am. Chem. Soc.*, 2014, **136**, 13818–13825.

11 W. Tress, N. Marinova, O. Inganäs, M. K. Nazeeruddin, S. M. Zakeeruddin and M. Graetzel, Predicting the Open-Circuit Voltage of $CH_3NH_3PbI_3$ Perovskite Solar Cells Using Electroluminescence and Photovoltaic Quantum Ef-ficiency Spectra: The Role of Radiative and Non-Radiative Recombination, *Adv. Energy Mater.*, 2015, **5**(3), 140812.

12 D. Bi, W. Tress, M. I. Dar, P. Gao, J. Luo, C. Renevier, K. Schenk, A. Abate, F. Giordano, J.-P. C. Baena, *et al.*, Efficient Luminescent Solar Cells Based on Tailored Mixed-Cation Perovskites, *Sci. Adv.*, 2016, **2**(1), e1501170.

13 M. Saliba, T. Matsui, K. Domanski, J.-Y. Seo, A. Ummadisingu, S. M. Zakeeruddin, J.-P. Correa-Baena, W. R. Tress, A. Abate, A. Hagfeldt, *et al.*, Incorporation of Rubidium Cations into Perovskite Solar Cells Improves Photovoltaic Performance, *Science*, 2016, **354**(6309), 206–209.

14 W. Tress, Perovskite Solar Cells on the Way to Their Radiative Efficiency Limit – Insights Into a Success Story of High Open-Circuit Voltage and Low Recombination, *Adv. Energy Mater.*, 2017, **7**(14), 1602358.

15 D. Meggiolaro, S. G. Motti, E. Mosconi, A. J. Barker, J. Ball, C. A. R. Perini, F. Deschler, A. Petrozza and F. De Angelis, Iodine chemistry determines the defect tolerance of lead-halide perovskites, *Energy Environ. Sci.*, 2018, **11**, 702–713.

16 J. Kang and L. W. Wang, High defect tolerance in lead halide perovskite $CsPbBr_3$, *J. Phys. Chem. Lett.*, 2017, **8**, 489–493.

17 H. Huang, M. I. Bodnarchuk, S. V. Kershaw, M. V. Kovalenko and A. L. Rogach, Lead halide perovskite nanocrystals in the research spotlight: Stability and defect tolerance, *ACS Energy Lett.*, 2017, **2**, 2071–2083.

18 W. Chu, Q. Zheng, O. V. Prezhdo, J. Zhao and W. A. Saidi, Low-frequency lattice phonons in halide perovskites explain high defect tolerance toward electron-hole recombination, *Sci. Adv.*, 2020, **6**, eaaw7453.

19 A. Zakutayev, C. M. Caskey, A. N. Fioretti, D. S. Ginley, J. Vidal, V. Stevanovic, E. Tea and S. Lany, Defect Tolerant Semiconductors for Solar Energy Conversion, *J. Phys. Chem. Lett.*, 2014, **5**, 1117–1125.

20 R. E. Brandt, V. Stevanovic, D. S. Ginley and T. Buonassisi, Identifying Defect-Tolerant Semiconductors with High Minority-Carrier Lifetimes: Beyond Hybrid Lead Halide Perovskites, *MRS Commun.*, 2015, **5**, 265–275.

21 M. Yavari, F. Ebadi, S. Meloni, Z. S. Wang, T. C.-J. Yang, S. Sun, H. Schwartz, Z. Wang, B. Niesen, J. Durantini, P. Rieder, K. Tvingstedt, T. Buonassisi, W. C. Choy, A. Filippetti, T. Dittrich, S. Olthof, J.-P. Correa-Baena and W. Tress, How far does the defect tolerance of lead-halide perovskites range? The example of Bi impurities introducing efficient recombination centers, *J. Mater. Chem. A*, 2019, **7**, 23838–23853.

22 M. Saba, M. Cadelano, D. Marongiu, F. Chen, V. Sarritzu, N. Sestu, C. Figus, M. Aresti, R. Piras, A. Geddo Lehmann, C. Cannas, A. Musinu, F. Quochi, A. Mura and

G. Bongiovanni, Correlated electron-hole plasma in organometal perovskites, *Nat. Commun.*, 2014, **5**, 5049.

23 T. J. Savenije, C. S. Ponseca, L. Kunneman, Jr, M. Abdellah, K. Zheng, Y. Tian, Q. Zhu, S. E. Canton, I. G. Scheblykin, T. Pullerits, A. Yartsev and V. Sundström, Thermally Activated Exciton Dissociation and Recombination Control the Carrier Dynamics in Organometal Halide Perovskite, *J. Phys. Chem. Lett.*, 2014, **5**, 2189–2194.

24 V. D'Innocenzo, G. Grancini, M. J. P. Alcocer, A. R. S. Kandada, S. D. Stranks, M. M. Lee, G. Lanzani, H. J. Snaith and A. Petrozza, Excitons versus free charges in organo-lead tri-halide perovskites, *Nat. Commun.*, 2014, **5**, 3586.

25 S. D. Stranks, V. M. Burlakov, T. Leijtens, J. M. Ball, A. Goriely and H. J. Snaith, Recombination Kinetics in Organic-Inorganic Perovskites: Excitons, Free Charge, and Subgap States, *Phys. Rev. Appl.*, 2014, **2**, 034007.

26 J. S. Manser and P. V. Kamat, Band filling with free charge carriers in organometal halide perovskites, *Nat. Photonics*, 2014, **8**, 737–743.

27 N. K. Noel, S. D. Stranks, A. Abate, C. Wehrenfennig, S. Guarnera, A.-A. Haghighirad, A. Sadhanala, G. E. Eperon, S. K. Pathak, M. B. Johnston, A. Petrozza, L. M. Herz and H. J. Snaith, Lead-free organic–inorganic tin halide perovskites for photovoltaic applications, *Energy Environ. Sci.*, 2014, **7**, 3061.

28 L. S. -Lujan, N. Espinosa, T. T. Larsen-Olsen, J. Abad, A. Urbina and F. C. Krebs, Tin- and Lead-Based Perovskite Solar Cells under Scrutiny: An Environmental Perspective, *Adv. Energy Mater.*, 2015, **5**, 1501119.

29 W. Ke, C. C. Stoumpos and M. G. Kanatzidis, "Unleaded" Perovskites: Status Quo and Future Prospects of Tin-Based Perovskite Solar Cells, *Adv. Mater*, 2019, **31**, 1803230.

30 Q. Tai, J. Cao, T. Wang and F. Yan, Recent advances toward efficient and stable tin-based perovskite solar cells, *EcoMat*, 2019, **1**, e12004.

31 S. Cai, Present Research Progress of Sn Halide Perovskite Solar Cells, *IOP Conf. Ser. Earth Environ. Sci.*, 2019, **242**, 022038.

32 L. Ma, F. Hao, C. C. Stoumpos, B. T. Phelan, M. R. Wasielewski and M. G. Kanatzidis, Carrier Diffusion Lengths of over 500 nm in Lead-Free Perovskite $CH_3NH_3SnI_3$ Films, *J. Am. Chem. Soc.*, 2016, **138**, 14750–14755.

33 R. L. Milot, G. E. Eperon, T. Green, H. J. Snaith, M. B. Johnston and L. M. Herz, Radiative Monomolecular Recombination Boosts Amplified Spontaneous Emission in $HC(NH_2)_2SnI_3$ Perovskite Films, *J. Phys. Chem. Lett.*, 2016, **7**, 4178–4184.

34 T. Handa, T. Yamada, H. Kubota, S. Ise, Y. Miyamoto and Y. Kanemitsu, Photocarrier Recombination and Injection Dynamics in Long-Term Stable Lead-Free $CH_3NH_3SnI_3$ Perovskite Thin Films and Solar Cells, *J. Phys. Chem. C*, 2017, **121**, 16158–21616.

35 H.-H. Fang, S. Adjokatse, S. Shao, J. Even and M. A. Loi, Long-lived hot-carrier light emission and large blue shift in formamidinium tin triiodide perovskites, *Nature Commun.*, 2018, **9**, 243.

36 R. L. Milot, M. T. Klug, C. L. Davies, Z. Wang, H. Kraus, H. J. Snaith, M. B. Johnston and L. M. Herz, The Effects of Doping Density and Temperature on the Optoelectronic Properties of Formamidinium Tin Triiodide Thin Films, *Adv. Mater.*, 2018, 1804506.

37 S. Kahmann and M. A. Loi, Hot carrier solar cells and the potential of perovskites for breaking the Shockley–Queisser limit, *J. Mater. Chem. C*, 2019, **7**, 2471.

38 G. Kim, H. Min, K. S. Lee, D. Y. Lee, S. M. Yoon and S. Il Seok, Impact of strain relaxation on performance of α-formamidinium lead iodide perovskite solar cells, *Science*, 2020, **370**, 108–112.

39 W. Liao, D. Zhao, Y. Yu, C. R. Grice, C. Wang, A. J. Cimaroli, P. Schulz, W. Meng, K. Zhu, R.-G. Xiong and Y. Yan, Lead-Free Inverted Planar Formamidinium Tin Triiodide Perovskite Solar Cells Achieving Power Conversion Efficiencies up to 6.22%, *Adv. Mater.*, 2016, **28**, 9333–9340.

40 W. Ke, C. C. Stoumpos, M. Zhu, L. Mao, I. Spanopoulos, J. Liu, O. Y. Kontsevoi, M. Chen, D. Sarma, Y. Zhang, M. R. Wasielewski and M. G. Kanatzidis, Enhanced photovoltaic performance and stability with a new type of hollow 3D perovskite {en}$FASnI_3$, *Sci. Adv.*, 2017, **3**, e1701293.

41 Z. Zhao, F. Gu, Y. Li, W. Sun, S. Ye, H. Rao, Z. Liu, Z. Bian and C. Huang, Mixed-Organic-Cation Tin Iodide for Lead-Free Perovskite Solar Cells with an Efficiency of 8.12%, *Adv. Sci.*, 2017, **4**, 1700204.

42 T.-B. Song, T. Yokoyama, C. C. Stoumpos, J. Logsdon, D. H. Cao, M. R. Wasielewski, S. Aramaki and M. G. Kanatzidis, Importance of Reducing Vapor Atmosphere in the Fabrication of Tin-Based Perovskite Solar Cells, *J. Am. Chem. Soc.*, 2017, **139**, 836–842.

43 W. Gao, C. Ran, J. Li, H. Dong, Bo Jiao, L. Zhang, X. Lan, X. Hou and Z. Wu, Robust Stability of Efficient Lead-Free Formamidinium Tin Iodide Perovskite Solar Cells Realized by Structural Regulation, *J. Phys. Chem. Lett.*, 2018, **9**, 6999–7006.

44 W. Ke, C. C. Stoumpos, I. Spanopoulos, M. Chen, M. R. Wasielewski and M. G. Kanatzidis, Diammonium Cations in the $FASnI_3$ Perovskite Structure Lead to Lower Dark Currents and More Efficient Solar Cells, *ACS Energy Lett.*, 2018, **3**, 1470–1476.

45 X. Liu, K. Yan, D. Tan, X. Liang, H. Zhang and W. Huang, Solvent Engineering Improves Efficiency of Lead-Free Tin-Based Hybrid Perovskite Solar Cells beyond 9%, *ACS Energy Lett.*, 2018, **3**, 2701–2707.

46 J. H. Heo, J. Kim, H. Kim, S. H. Moon, S. Hyuk Im and Ki-Ha Hong, Roles of SnX_2 (X = F, Cl, Br) Additives in Tin-Based Halide Perovskites toward Highly Efficient and Stable Lead-Free Perovskite Solar Cells, *J. Phys. Chem. Lett.*, 2018, **9**, 6024–6603.

47 Md. E. Kayesh, T. H. Chowdhury, K. Matsuishi, R. Kaneko, S. Kazaoui, J.-J. Lee, T. Noda and A. Islam, Enhanced Photovoltaic Performance of $FASnI_3$-Based Perovskite Solar

Cells with Hydrazinium Chloride Coadditive, *ACS Energy Lett.*, 2018, **3**, 1584–1589.

48 S. Shao, J. Liu, G. Portale, H.-H. Fang, G. R. Blake, G. H. ten Brink, L. Jan Anton Koster and M. A. Loi, Highly Reproducible Sn-Based Hybrid Perovskite Solar Cells with 9% Efficiency, *Adv. Energy Mater.*, 2018, **8**, 1702019.

49 S. Adjokatse, S. Kahmann, H. Duim and M. A. Loi, Effects of strontium doping on the morphological, structural, and photophysical properties of $FASnI_3$ perovskite thin films, *APL Mater.*, 2019, **7**, 031116.

50 E. Jokar, C.-H. Chien, C.-M. Tsai, A. Fathi, E. W. Guang and D. Robust, Tin-Based Perovskite Solar Cells with Hybrid Organic Cations to Attain Efficiency Approaching 10%, *Adv. Mater.*, 2019, **31**, 1804835.

51 M. A. Kamarudin, D. Hirotani, Z. Wang, K. Hamada, K. Nishimura, Q. Shen, T. Toyoda, S. Iikubo, T. Minemoto, K. Yoshino and S. Hayase, Suppression of Charge Carrier Recombination in Lead-Free Tin Halide Perovskite via Lewis Base Post-treatment, *J. Phys. Chem. Lett.*, 2019, **10**, 5277–5283.

52 M. Liao, B.-B. Yu, Z. Jin, W. Chen, Y. Zhu, X. Zhang, W. Yao, T. Duan, I. Djerdj and Z. He, Efficient and Stable $FASnI_3$ Perovskite Solar Cells with Effective Interface Modulation by Low-Dimensional Perovskite Layer, *ChemSusChem*, 2019, **12**, 1–9.

53 X. Meng, J. Lin, X. Liu, X. He, Y. Wang, T. Noda, T. Wu, X. Yang and L. Han, Highly Stable and Efficient $FASnI_3$-Based Perovskite Solar Cells by Introducing Hydrogen Bonding, *Adv. Mater.*, 2019, **31**, 1903721.

54 S. Kahmann, S. Shao and M. A. Loi, Cooling, Scattering, and Recombination—The Role of the Material Quality for the Physics of Tin Halide Perovskites, *Adv. Funct. Mater.*, 2019, **29**, 1902963.

55 A. Filippetti, C. D. Pemmaraju, S. Sanvito, P. Delugas, D. Puggioni and V. Fiorentini, *Phys. Rev. B: Condens. Matter Mater. Phys.*, 2011, **84**, 195127.

56 D. Puggioni, A. Filippetti and V. Fiorentini, Ordering and multiple phase transitions in ultra-thin nickelate superlattices, *Phys. Rev. B: Condens. Matter Mater. Phys.*, 2012, **86**, 195132.

57 P. Delugas, A. Filippetti, A. Gadaleta, I. Pallecchi, D. Marré and V. Fiorentini, Large band offset as driving force of 2-dimensional electron confinement: the case of $SrTiO_3$/$SrZrO_3$ interface, *Phys. Rev. B: Condens. Matter Mater. Phys.*, 2013, **88**, 115304.

58 P. Delugas, A. Filippetti, M. Verstraete, I. Pallecchi, D. Marrè and V. Fiorentini, Doping-induced dimensional crossover and thermopower burst in Nb-doped $SrTiO_3$ superlattices, *Phys. Rev. B: Condens. Matter Mater. Phys.*, 2013, **88**, 045310.

59 P. Delugas, V. Fiorentini, A. Mattoni and A. Filippetti, Intrinsic origin of two-dimensional electron gas at the (001) surface of $SrTiO_3$, *Phys. Rev. B: Condens. Matter Mater. Phys.*, 2015, **91**, 115315.

60 X. Chang, D. Marongiu, V. Sarritzu, N. Sestu, Q. Wang, S. Lai, A. Mattoni, A. Filippetti, F. Congiu, A. Geddo Lehmann, F. Quochi, M. Saba, A. Mura and G. Bongiovanni, Layered Germanium Hybrid Perovskite Bromides: Insights from Experiments and First-Principles Calculations, *Adv. Funct. Mater.*, 2019, 1903528.

61 F. Liu, D. Marongiu, R. Pau, V. Sarritzu, Q. Wang, S. Lai, A. G. Lehmann, F. Quochi, M. Saba, A. Mura, G. Bongiovanni, A. Mattoni, C. Caddeo, A. Bosin and A. Filippetti, Ag/In lead-free double perovskites, *EcoMat*, 2020, **2**(1), e12017.

62 I. Borriello, G. Cantele and D. Ninno, Ab initio investigation of hybrid organic-inorganic perovskites based on tin halides, *Phys. Rev. B: Condens. Matter Mater. Phys.*, 2008, **77**, 235214.

63 Zi-Q. Ma, H. Pan and P. K. Wong, A First-Principles Study on the Structural and Electronic Properties of Sn-Based Organic–Inorganic Halide Perovskites, *J. Electron. Mater.*, 2016, **45**(No. 11).

64 P. Umari, E. Mosconi and F. De Angelis, Relativistic GW calculations on $CH_3NH_3PbI_3$ and $CH_3NH_3SnI_3$ Perovskites for Solar Cell Applications, *Sci. Rep.*, 2014, **4**, 4467.

65 T. Shi, H.-S. Zhang, W. Meng, Q. Teng, M. Liu, X. Yang, Y. Yan, H.-L. Yip and Yu-J. Zhao, Effects of organic cations on the defect physics of tin halide perovskites, *J. Mater. Chem. A*, 2017, **5**, 15124.

66 D. Meggiolaro, F. Ambrosio, E. Mosconi, A. Mahata and F. De Angelis, Polarons in Metal Halide Perovskites, *Adv. Energy Mater.*, 2019, 1902748.

67 J. Heyd, G. E. Scuseria and M. Ernzerhof, *J. Chem. Phys.*, 2003, **118**, 8207–8215.

68 T. Archer, C. D. Pemmaraju, S. Sanvito, C. Franchini, J. He, A. Filippetti, P. Delugas, D. Puggioni, V. Fiorentini, R. Tiwari and P. Majumdar, Exchange interactions and magnetic phases of transition metal oxides: benchmarking advanced ab initio methods, *Phys. Rev. B: Condens. Matter Mater. Phys.*, 2011, **84**, 115114.

69 L. G. Ferreira, M. Marques and L. K. Teles, *Phys. Rev. B: Condens. Matter Mater. Phys.*, 2008, **78**, 125116.

70 D. Guedes-Sobrinho, I. Guilhon, M. Marques and L. K. Teles, Relativistic DFT-1/2 Calculations Combined with a Statistical Approach for Electronic and Optical Properties of Mixed Metal Hybrid Perovskites, *J. Phys. Chem. Lett.*, 2019, **10**, 4245–4251.

71 F. Valadares, I. Guilhon, L. K. Teles and M. Marques, Electronic Structure Panorama of Halide Perovskites: Approximated DFT-1/2 Quasiparticle and Relativistic Corrections, *J. Phys. Chem. C*, 2020, **124**, 18390–18400.

72 S. Kahmann, O. Nazarenko, S. Shao, O. Hordiichuk, M. Kepenekian, J. Even, M. V. Kovalenko, G. R. Blake and M. A. Loi, Negative Thermal Quenching in $FASnI_3$ Perovskite Single Crystals and Thin Films, *ACS Energy Lett.*, 2020, **5**, 2512–2519.

73 F. Matusalem, M. Marques, L. K. Teles, A. Filippetti and G. Cappellini, Electronic properties of fluorides by efficient approximated quasiparticle DFT-1/2 and PSIC methods: BaF_2, CaF_2 and CdF_2 as test cases, *J. Phys.: Condens. Matter*, 2018, **30**, 365501.

74 Inquires about the use of the PWSIC code can be addressed by email to the corresponding author.

75 D. Vanderbilt, Soft self-consistent pseudopotentials in a generalized eigenvalue formalism, *Phys. Rev. B: Condens. Matter Mater. Phys.*, 1990, **41**, 7892–7895.
76 W. Van Roosbroeck and W. Shockley, Photon-Radiative Recombination of Electrons and Holes in Germanium, *Phys. Rev.*, 1954, **94**, 1558–1560.
77 W. Shockley and H. J. Queisser, Detailed Balance Limit of Efficiency of P-N Junction Solar Cells, *J. Appl. Phys.*, 1961, **32**, 510.
78 A. Filippetti, P. Delugas and A. Mattoni, Radiative Recombination and Photoconversion of Methylammonium Lead Iodide Perovskite by First Principles: Properties of an Inorganic Semiconductor within a Hybrid Body, *J. Phys. Chem. C*, 2014, **118**, 24843–24853.
79 A. Filippetti, C. Caddeo, P. Delugas and A. Mattoni, Photoluminescence, optical gain, and lasing threshold in $CH_3NH_3Pb_3$ methylammonium lead-halide perovskites by ab initio calculations, *J. Mater. Chem. C*, 2017, **5**, 12758–12768, DOI: 10.1039/C7TC04717G.
80 C. C. Stoumpos, C. D. Malliakas and M. G. Kanatzidis, Semiconducting tin and lead iodide perovskites with organic cations: phase transitions, high mobilities, and near-infrared photoluminescent properties, *Inorg. Chem.*, 2013, **52**, 9019–9038.
81 T. Baikie, Y. Fang, J. M. Kadro, M. Schreyer, F. Wei, S. G. Mhaisalkar, M. Graetzel and T. J. White, Synthesis and crystal chemistry of the hybrid perovskite $(CH_3NH_3)PbI_3$ for solid-state sensitised solar cell applications, *J. Mater. Chem. A*, 2013, **1**, 5628–5641.
82 A. Filippetti, A. Mattoni, C. Caddeo, M. I. Saba and P. Delugas, Low Electron-Polar Optical Phonon Scattering as a Fundamental Aspect of Carrier Mobility in Methylammonium Lead Halide $CH_3NH_3PbI_3$ Perovskites, *Phys. Chem. Chem. Phys.*, 2016, **18**, 15352–15362.
83 G. Giorgi, J.-I. Fujisawa, H. Segawa and K. Yamashita, Small Photocarrier Effective Masses Featuring Ambipolar Transport in Methylammonium Lead Iodide Perovskite: A Density Functional Analysis, *J. Phys. Chem. Lett.*, 2013, **4**, 4213–4216.
84 M. Bokdam, T. Sander, A. Stroppa, S. Picozzi, D. D. Sarma, C. Franchini and G. Kresse, Role of Polar Phonons in the Photo Excited State of Metal Halide Perovskites, *Sci. Rep.*, 2016, **6**, 28618.
85 C. Wehrenfennig, G. E. Eperon, M. B. Johnston, H. J. Snaith and L. M. Herz, High Charge Carrier Mobilities and Lifetimes in Organolead Trihalide Perovskites, *Adv. Mater.*, 2014, **26**, 1584–1589.
86 C. Motta, F. El-Mellouhi and S. Sanvito, Charge Carrier Mobility in Hybrid Halide Perovskites, *Sci. Rep.*, 2015, **5**, 12746.
87 T. M. Brenner, D. A. Egger, L. Kronik, G. Hodes and D. Cahen, Hybrid organic–inorganic perovskites: low-cost semiconductors with intriguing charge-transport properties, *Nat. Rev. Mater.*, 2016, **1**, 15007.
88 M. Karakus, S. A. Jensen, F. D'Angelo, D. Turchinovich, M. Bonn and E. Canovas, Phonon–Electron Scattering Limits Free Charge Mobility in Methylammonium Lead Iodide Perovskites, *J. Phys. Chem. Lett.*, 2015, **6**, 4991–4996.
89 S. De Wolf, J. Holovsky, S.-J. Moon, P. Löper, B. Niesen, M. Ledinsky, F.-J. Haug, J.-H. Yum and C. Ballif, Organometallic Halide Perovskites: Sharp Optical Absorption Edge and Its Relation to Photovoltaic Performance, *J. Phys. Chem. Lett.*, 2014, **5**, 1035–1039.
90 B. E. Treml and T. Hanrath, Quantitative Framework for Evaluating Semitransparent Photovoltaic Window, *ACS Energy Lett.*, 2016, **1**, 391–394.
91 A. A. F. Husain, W. Z. W. Hasan, S. Shafie, M. N. Hamidon and S. S. Pandey, A review of transparent solar photovoltaic technologies, *Renew. Sustain. Energy Rev.*, 2018, **94**, 779–791.
92 Z. Hu, Z. Wang and F. Zhang, Semitransparent polymer solar cells with 9.06% efficiency and 27.1% average visible transmittance obtained by employing a smart strategy, *J. Mater. Chem. A*, 2019, **7**, 7025.
93 D. Marongiu, S. Lai, V. Sarritzu, E. Pinna, G. Mula, M. L. Mercuri, M. Saba, F. Quochi, A. Mura and G. Bongiovanni, Bifacial Diffuse Absorptance of Semitransparent Microstructured Perovskite Solar Cells, *ACS Appl. Mater. Interfaces*, 2019, **11**, 10021–10027.
94 C. Roldan-Carmona, O. Malinkiewicz, R. Betancur, G. Longo, C. Momblona, F. Jaramillo, L. Camacho and H. J. Bolink, High efficiency single-junction semitransparent perovskite solar cells, *Energy Environ. Sci.*, 2014, **7**, 2968.
95 C. D. Bailie, M. G. Christoforo, J. P. Mailoa, *et al.*, Semi-transparent perovskite solar cells for tandems with silicon and CIGS, *Energy Environ. Sci.*, 2014, **8**, 956–963.
96 C. J. Traverse, R. Pandey, M. C. Barr and R. R. Lunt, Emergence of highly transparent photovoltaics for distributed applications, *Nat. Energy*, 2017, **2**, 849–860.
97 J. Jean, T. S. Mahony, D. Bozyigit, M. Sponseller, J. Holovsky, M. G. Bawendi and V. Bulovic, Radiative Efficiency Limit with Band Tailing Exceeds 30% for Quantum Dot Solar Cells, *ACS Energy Lett.*, 2017, **2**, 2616–2624.

